Efficient photocapacitors via ternary hybrid photovoltaic optimization for photostimulation of neurons

SHASHI BHUSHAN SRIVASTAVA,[1] RUSTAMZHON MELIKOV,[1]
ERDOST YILDIZ,[2] MERTCAN HAN,[1] AFSUN SAHIN,[2,3] AND SEDAT
NIZAMOGLU[1,4,*]

[1]*Department of Electrical and Electronics Engineering, Koc University, Istanbul 34450, Turkey*
[2]*Koc University Research Center for Translational Medicine, Koc University, Istanbul 34450, Turkey*
[3]*Department of Ophthalmology, Medical School, Koc University, Istanbul 34450, Turkey*
[4]*Graduate School of Biomedical Sciences and Engineering, Koc University, Istanbul 34450, Turkey*
*snizamoglu@ku.edu.tr

Abstract: Optoelectronic photoelectrodes based on capacitive charge-transfer offer an attractive route to develop safe and effective neuromodulators. Here, we demonstrate efficient opto-electronic photoelectrodes that are based on the incorporation of quantum dots (QDs) into poly(3-hexylthiophene-2,5-diyl) (P3HT) and [6,6]-Phenyl-C61-butyric acid methyl ester (PCBM) bulk heterojunction. We control the performance of the photoelectrode by the blend ratio, thickness, and nanomorphology of the ternary bulk heterojunction. The optimization led to a photocapacitor that has a photovoltage of 450 mV under a light intensity level of 20 mW.cm^{-2} and a responsivity of 99 mA/W corresponding to the most light-sensitive organic photoelectrode reported to date. The photocapacitor can facilitate action potential generation by hippocampal neurons via burst waveforms at an intensity level of 20 mW.cm^{-2}. Therefore, the results point to an alternative direction in the engineering of safe and ultra-light-sensitive neural interfaces.

1. Introduction

Optoelectronic photoelectrodes offer high potential for wireless and safe photostimulation of neurons [1–12]. They have been started to be investigated for retinal implants that enabled restoration of vision *in-vivo* [13,14]. The management of charge-transfer mechanisms at the electrode-electrolyte interfaces and transduction of low-intensity light levels to safe currents can advance the control of neuron activity and facilitate retina-like highly sensitive neurointerfaces in the future. In terms of the charge-transfer mechanisms, optoelectronic materials can generate currents based on capacitive or Faradaic mechanisms [15]. Capacitive charge-transfer mechanism can modulate the membrane potential without any direct charge movement to the electrolyte [1,10,16–18]. The objective for pure capacitive mechanism of charge injection is to maintain electric potential in such a way that it does not induce irreversible redox reactions, which are responsible for the permanent damage of the biological media, neuron cell, and corrosion of the neurostimulator itself [1,10]. Eventually, the photoelectrode design becomes important to produce safe capacitive currents. At the same time, realization of operation at low-light intensity levels can facilitate efficient communication with living systems without any heat-induced side effects [19].

   Polymeric semiconductors are one of the promising materials for optoelectronic photoelectrodes due to its inherent properties such as solution processability, biocompatibility, flexibility, and easy handling [14,20,21]. So far, optically-active substrates using different conjugated polymer material systems such as P3HT, P3HT:PCBM, P3HT:PbS-QDs:PCBM, P3OT:N2200, PDPP3T:PCBM, and P3HT:N2200 were demonstrated for photostimulation [20–25]. To reach

higher device performance levels, the organic polymer, polymer-small molecule (donor-acceptor) bulk heterojunction thin films and the performance-enhancing additives require intense process optimization to reach the high performing morphology and structure [26–29]. Inspired by the importance of the process optimization for solution-processed hybrid photovoltaics, we systematically investigated and optimized the nanomorphology, composition and thickness of P3HT:PCBM and PbS QD incorporated ternary heterojunctions for efficient and safe photovoltaic neural interfaces that can generate stimulating capacitive currents at a responsivity level of 99 mA/W.

2. Materials and methods

2.1. Materials and photoelectrode fabrication

The photoelectrode presented in this work used poly(3-hexylthiophene-2,5-diyl) (P3HT), [6,6]-Phenyl-C61-butyric acid methyl ester (PCBM), and colloidal lead sulfide quantum dots (PbS QDs) in toluene, which were used as received from Sigma Aldrich without any modification. The size of the PbS QDs with oleic acid as a ligand is 3.7 nm [30,31]. The energy levels of each materials were calculated from cyclic voltammetry measurement as reported in our previous work and are close to the literature values [30,32,33].

To optimize the photoelectrode performance, we fabricated binary (P3HT:PCBM) and ternary (P3HT:PbS QDs:PCBM) photoelectrodes with diverse conditions. Firstly, the indium tin oxide (ITO) coated glass substrates were cleaned sequentially by sonication in soap solution, de-ionized water, acetone, and iso-propanol. The cleaned substrates were dried in oven at 100 °C. Before coating of zinc oxide (ZnO), the substrates were kept in UV-Ozone cleaner for 20 min. The 0.45M ZnO precursor solution was prepared by dissolving zinc acetate di-hydrate in 2-methoxy ethanol and ethanolamine through sonication of 15 min at 50 °C. The clear ZnO precursor solution was spin coated on ITO substrates at 2000 rpm for 60 sec. Further, the coated substrates were annealed at 250 °C temperature on hot plate in ambient. The photoactive solutions were prepared by dissolving P3HT:PCBM or P3HT:PbSQDs:PCBM in 1,2-dichlorobenzene in different compositions. Then, photoactive layers were coated on ZnO thin film by spin coating keeping constant thickness for the different compositions. The photoactive layer was annealed at 155 °C to get the optimized nanomorphology of the bulk heterojunction. Further, the active layers with varying thicknesses were prepared for the optimized composition to confirm the final photoelectrode thickness. The thickness of various layers was confirmed by SEM cross-section image. The thin film morphology of the active layers was measured using atomic force microscopy (Bruker Instruments).

2.2. Photocurrent measurement

The photostimulation was performed on a set-up comprising of Olympus T2 upright microscope and was placed inside a Faraday cage to prevent electrical noises. EPC 800 patch clamp amplifier (HEKA Elektronik, Lambrecht, Germany) was used for the photocurrent measurements. For the light stimulation, we used blue light emitting diodes (LED) (M450LP1, Thorlabs, NJ, USA) with nominal wavelength of 445 nm, green LED (M530L3, Thorlabs, NJ, USA) with nominal wavelength of 530 nm, and red LED with nominal wavelength of 630 nm. All LEDs were driven by DC2200 - High-Power 1-Channel LED Driver with Pulse Modulation (Thorlabs, NJ, USA). The FWHM of blue, green and red-light spectrum are 16.7 nm, 33.3 nm, and 13.4 nm, respectively. A power meter (Newport 843-R) was used to measure the precise power of light reaching at the interface. The illumination was focused on water immersion objective (40x/0.8 W, inf/0/FN 26.5) from the ITO (a transparent electrode) side of the photoelectrode. The arrangement of the photocurrent measurement set-up, in which the ITO electrode was grounded directly to the amplifier was similar to the previous report [1].

2.3. Electrophysiology measurement

EPC 800 patch clamp amplifier (HEKA Elektronik, Lambrecht, Germany) was used for the electrophysiology measurements. The pulled patch pipettes of 8-12 MΩ were used to perform the whole-neuron cells under Giga-Ohm seal. Extracellular solution (Artificial Cerebrospinal Fluid, aCSF) is prepared as; 140 mM NaCl, 3 mM KCl, 1 mM $MgCl_2$, 2 mM $CaCl_2$, 10 mM HEPES, 10 mM Glucose. Osmolarity adjusted to 290 mOsm and pH adjusted to 7.4 with NaOH. Internal cellular solution (ICS) is prepared as; 140 mM KCl, 2 mM $MgCl_2$, 10 mM HEPES, 10 mM EGTA, 2 mM Mg-ATP. Osmolarity adjusted to 270 mOsm and pH adjusted to 7.3 with KOH. ICS was used to fill the patch pipettes during the measurement. Olympus T2 upright microscope and a digital camera was used in the electrophysiology set-up to monitor the cells like the photocurrent measurements. The stimulations of the primary hippocampal neurons were effective up to 30 minutes and after that they lost their excitability because of the damage by patched microelectrode.

### 2.4. Primary hippocampal neuron isolation and culture

Hippocampal regions were extracted from decapitated E15-E17 Wistar Albino rats and were placed immediately in ice-cold Hank's Balanced Salt Solution (HBSS, Thermo Fisher Scientific, MA, USA). The hippocampi were incubated in % 0.25 Trypsin-EDTA solution (Thermo Fisher Scientific, MA, USA) with %2 DNase-I supplement (NeoFroxx, Einhausen, Germany) for 20 minutes in a 37 ^{0}C incubator. Then the cells were centrifuged and the supernatant was changed with Dulbecco's Modified Eagle Medium/Nutrient Mixture F-12 (DMEM/F12 Thermo Fisher Scientific, MA, USA) supplemented with %10 fetal bovine serum (FBS, Heat Inactivated, GE Healthcare, IL, USA) and %1 penicillin/streptomycin (Thermo Fisher Scientific, MA, USA). DMEM/F12 was removed and Neurobasal Medium (NBM, Thermo Fisher Scientific, MA, USA) supplemented with B27, L-glutamine, β-mercaptoethanol, glutamate (Thermo Fisher Scientific, MA, USA) was added to the cell pellet. The cells were triturated and were passed through a 70 μm cell strainer. The homogenous cell solution was seeded in poly-D-lysine (PDL, Sigma-Aldrich, MO, USA) coated substrates. After 3-days incubation of cells on substrates in a 37 ^{0}C incubator with %5 carbon dioxide, the media of the cells on substrates were changed with NBM supplemented with cytosine arabinoside (Sigma-Aldrich, MO, USA) to inhibit growth of glial cells. After 24-hour incubation with cytosine arabinoside, the media were changed with NBM. Therefore, for maturation of primary hippocampal neural cells, the cells on substrates have been incubated in NBM between 3 to 5 days before patch clamp experiments [34–36]. Then, the hippocampal neurons were used to culture on photoelectrode substrates for future experiments.

3. Results and discussion

3.1. Concept and optimization of P3HT:PCBM blend

The photoactive layer is composed of P3HT, PbS core QDs, and PCBM (Fig. 1(a)). The ternary-blend advantageously forms a stepwise energy profile for effective photovoltaic effect (Fig. 1(b)). After the light is absorbed by the photoactive layer, the generated excitons dissociate, and the electron and hole move towards the PCBM and P3HT in the photoactive layer, respectively. To produce capacitive photocurrent, the photoactive layer is deposited on top of the ITO/ZnO layers [1]. This further allows the accumulation of the electron toward the ITO/ZnO and lead to sufficient carrier lifetime for holes to induce capacitive photocurrent.

To maximize the performance by the photoelectrode, we started the optimization with the P3HT:PCBM ratio of the bulk heterojunction. The photocurrents were characterized by using a patch-clamp electrophysiology set-up under the 1 mW.cm^{-2} optical excitation level at the wavelength of 445 nm. For that a micropipette was immersed into an aCSF electrolyte solution and positioned close to the surface of photoelectrode. The photocurrent values of the photoelectrodes
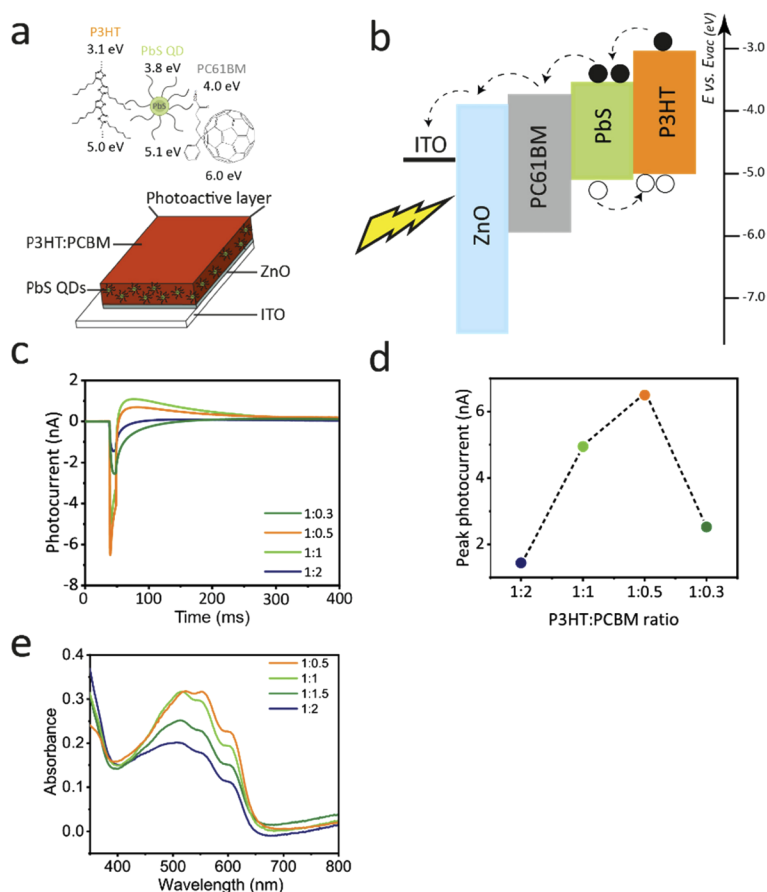
Fig. 1. (a) Top panel: Chemical structures of P3HT, PbS QDs, and PCBM and their respective HOMO and LUMO energy levels. Lower panel: Schematic showing the ternary (P3HT: PbS QDs: PCBM) optoelectronic photoelectrode architecture. (b) Energy levels of the photoelectrode and movement of the photogenerated charge carriers. (c) Photocurrent of binary photoelectrodes with varying PCBM contents measured in a patch-clamp electrophysiology system. (d) Peak photocurrent for the photoelectrodes (without QDs) as a function of the binary blend with various PCBM contents. (e) UV-vis absorption spectra of binary blend films with various P3HT:PCBM contents.

were measured for different weight percentage of PCBM loading ratio in the P3HT:PCBM blend. After a 10-ms light pulse, the spikes after the onset and offset of illumination points out a capacitive current generation by the photoelectrode (Fig. 1(c)). The P3HT:PCBM ratio of 1:2 shows a peak current of 1.43 nA (Fig. 1(d)), and while the PCBM ratio is decreased, the maximum photocurrent of 6.49 nA was observed with P3HT:PCBM ratio of 1:0.5.

The absorption spectrum of P3HT:PCBM thin film with the PCBM weight ratio of 1:0.5 is shown in Fig. 1(e). The two peaks at 518 nm and 552 nm can be attributed to the π-π* transition of the crystallized P3HT because of thermal annealing, whereas the shoulder peak at 604 nm is due to the inter-chain interaction of P3HT polymers [37,38]. However, the significant reduction in absorption spectra of the blend thin films was observed sequentially with increasing weight ratio of PCBM. We attribute the weaker absorbance due to the reduced absorption of P3HT polymer in the PCBM molecular blend. For good photovoltaic effect, while having enhanced

light harvesting, improved charge carrier transport is a critical parameter. Hence, this indicates that interpenetrating nanomorphology of P3HT:PCBM bulk heterojunction is an important factor.

The effect of P3HT:PCBM surface morphology on photocurrent is investigated for different thicknesses. The Fig. 2(a) shows the AFM images of 5 μm × 5 μm area of P3HT:PCBM surfaces with the optimized binary ratio of 2:1 on ITO/ZnO coated glass substrates. A high degree of average roughness (6.02 nm) is observed on the surface of the 210 nm thick films with bigger clusters. The photoelectrode at 210-nm thickness generates a capacitive current of 4.96 nA (Fig. 2(b) and 2(c)). On the contrary, the surfaces roughness significantly reduces, while the thickness decreases. The morphology of the P3HT:PCBM thin film with 155 nm thickness provides better intermixed nanomorphology with smaller domains, which lead to enhanced exciton dissociation [39]. In addition, lower roughness can also help in reduction of leakage current at the thin film interface. Hence, the maximum current level of 6.41 nA is observed at this thickness level. The further decrease in the thickness resulted into smoother, but inhomogeneous surface, which led to 4.14 and 4.01 nA current levels for the thickness of 85 and 60 nm, respectively. Hence, for all the investigated thickness levels capacitive current were observed, and beside strong absorption of the visible light, the nanomorphology at the thickness level of ∼ 155 nm allowed for generation of high levels of currents.
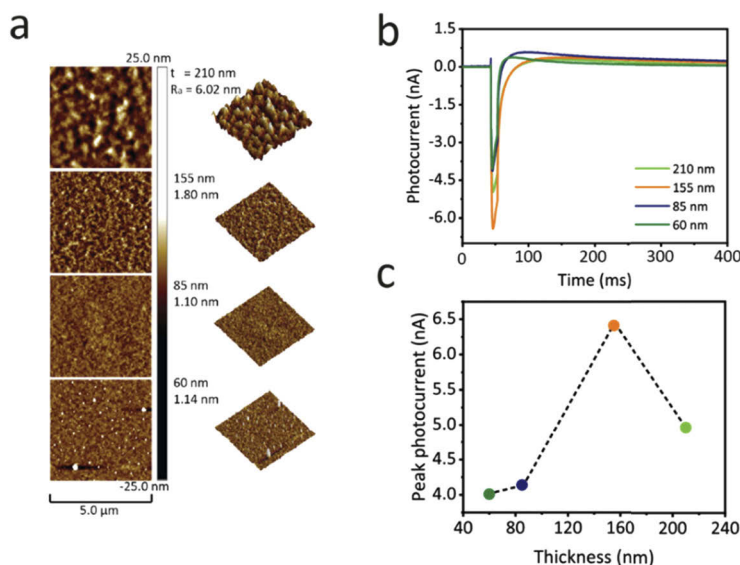

Fig. 2. (a) Atomic force microscopy (5 μm × 5 μm) of binary films (left: 2D views; right: 3D views) with various thin film thicknesses (t) in tapping-mode. R_a shows the average surface roughness. (b) Photocurrent of binary photoelectrodes with various thin film thicknesses. (c) Peak photocurrent for the binary photoelectrodes as a function of various thin film thicknesses.

3.2. Optimization of colloidal PbS QDs in P3HT:PCBM blend

PbS QD ratio is investigated in the host optimum P3HT:PCBM polymeric matrix to maximize the optical response of the photoelectrode. For that, PbS QDs up to 20 w% with respect to P3HT are incorporated into P3HT:PCBM and the resultant photocurrents are measured. All the PbS QDs and P3HT:PCBM blends showed capacitive currents (Fig. 3(a)). Incorporation of 5% PbS QDs led to a peak photocurrent of 7.9 nA, and the maximum photocurrent of 8.5 nA is observed in the biological media for the photoelectrode having 10% PbS QDs in the binary blend of P3HT:PCBM (Fig. 3(b)). This corresponds to a 25% increase of the peak current

level in comparison with the bulk heterojunction based photoelectrode without quantum dots. Figure 3(c) shows the normalized UV-vis absorption spectra of the binary (P3HT:PCBM) and ternary (P3HT:PbS QDs:PCBM) blend thin films. Although PbS QDs absorbs in visible and IR region, limited change in absorption was observed due to the small loading percentage of the PbS QDs in the P3HT:PCBM bulk heterojunction. We investigated the thin film morphology of the ternary blend and compared it with optimized thin film morphology of the binary blend (P3HT:PCBM). Compared to the binary blend thin film, high intermixed and low roughness films are obtained (Fig. 3(d) and 3(e)) showing the main reason of the increased photocurrent.
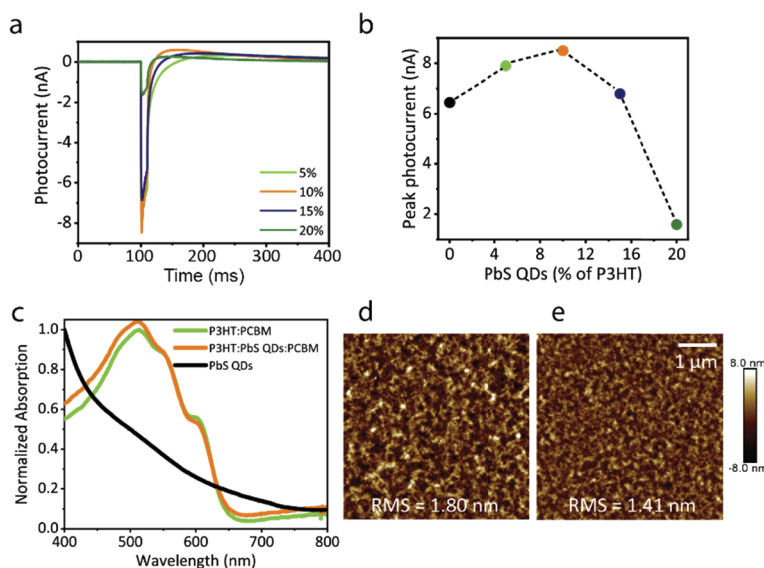

Fig. 3. (a) The analysis of the photocurrent obtained from the ternary (P3HT:PbS QDs:PCBM) biointerfaces having different QD concentration with respect to P3HT. (b) Peak photocurrents for the ternary biointerfaces as a function of the proportion of PbS QDs relative to P3HT. (c) UV-vis absorption spectra of the PbS QDs (in-solution), optimized binary and ternary blend films. The normalization was done with respect to absorption maxima within the spectral range. (d) Tapping-mode AFM ($5 \times 5\,\mu m$) of optimized binary blend film. (e) Tapping-mode AFM ($5 \times 5\,\mu m$) of optimized ternary blend film.

3.3. Electrochemical photoresponse

One important measure showing the ability of the effective photostimulation is the quantification of photocurrent per unit area. We measured the electrochemical photoresponse of the optimized photoelectrode under the three-probe configuration that allow understanding the actual potential of the photoelectrode in terms of photocurrent and photovoltage. In this configuration (Fig. 4(a)), the ITO electrode is used as working electrode, the platinum electrode is used as counter electrode and the Ag/AgCl as reference electrode. The measurement was done in the fast chronoamperometry mode to increase signal-to-noise ratio. During the measurement, no voltage was applied to the working electrode and current was monitored over time under light-pulse of 5 ms with 20 mW.cm^{-2} intensity illuminated on the photoactive area of 1 cm^2, which is exposed to the aCSF electrolyte. Figure 4(b) shows the optical spectrum of the blue, green, and red LEDs with optical power density of 20 mW.cm^{-2}. Figure 4(c) shows the photovoltage of the photoelectrode measured between working electrode (ITO) and counter electrode (Pt) using pulsed (5 ms) illuminations of blue, green, and red lights. The ternary photoelectrode can generate about 450 mV of photovoltage for green light pulse, which is more than the previous

state of the art reports [2,40–42]. For blue and red spectral windows, we also observe the photovoltages of 381 and 367 mV, respectively. Corresponding to the maximum photovoltage, the photocapacitive current (Fig. 4(d)) is found 1.98 mA.cm^{-2} for light intensity level of 20 mW.cm^{-2} under green illumination. This corresponds to a high-level responsivity of 99 mA/W. We also measure the capacitive currents for blue and red light as well. The photocurrents are 0.74 and 0.47 for blue and red, respectively, which match well with the absorption response of ternary blend (Fig. 4(d) inset). During the initial spike, the total charge injection amount corresponds to 0.61 μC.cm^{-2} evidencing the effective neuromodulation ability via capacitive charge-transfer mechanism.
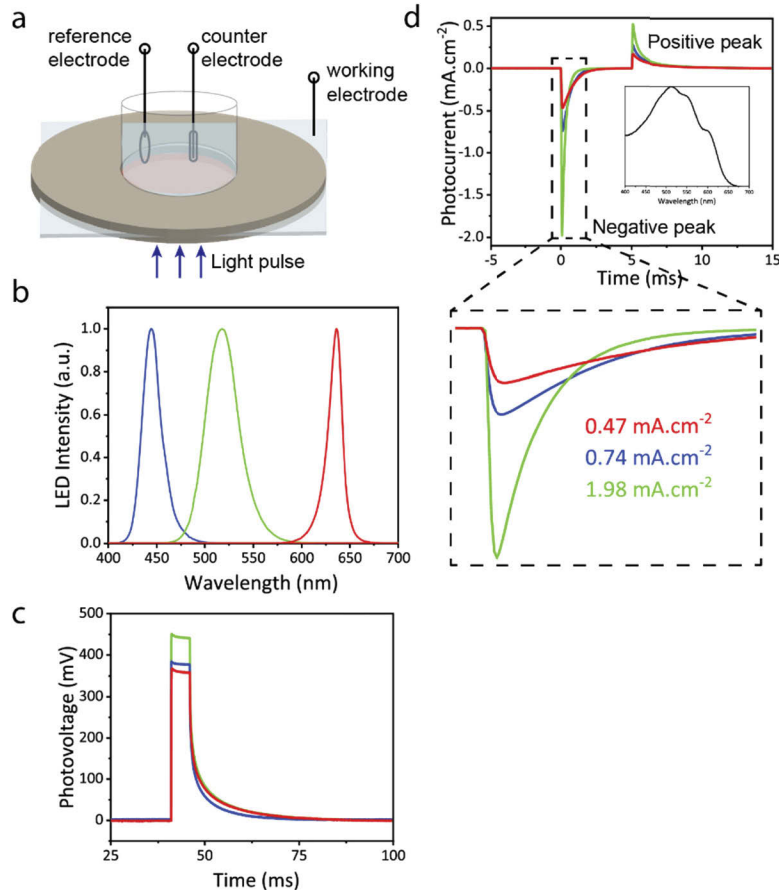
Fig. 4. (a) Schematic illustrating the electrochemical measurement configuration of the photoelectrode in an aCSF solution. A LED (pulsed) is used to illuminate and activate the photoelectrodes. (b) Optical spectrum of blue, green, and red LEDs with optical power level of 20 mW.cm^{-2}. (c) Photovoltage measurement under blue light (5 ms, 445 nm), green light (5 ms, 530 nm), and red light (5 ms, 630 nm). (d) The corresponding photocurrent obtained under red, green, and blue light illumination (5 ms pulse, 20 mW.cm^{-2} light intensity). Inset shows the peak photocurrent when the light is tuned ON.

3.4. Photostimulation of primary hippocampal cells

For photostimulation experiments we cultured primary hippocampal neurons that is extracted from decapitated E15-E17 Wistar Albino rats on the optimized photoelectrode. The electrophysiological
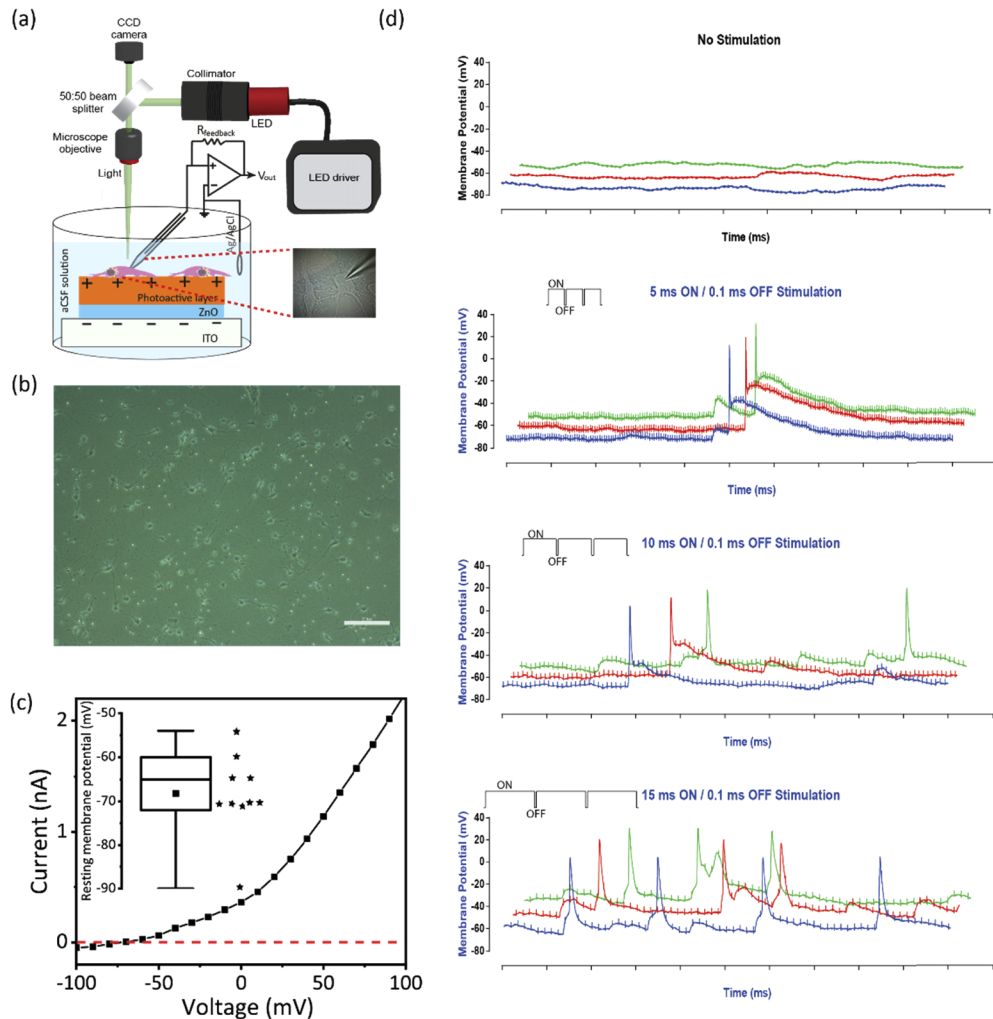
Fig. 5. (a) Schematic of the whole-cell patch clamp recoding configuration of the photoelectrode in free-standing mode. A LED at far field is used to illuminate and activate the photoelectrode. Primary hippocampal neurons were incubated for 3 days on the photoelectrode and afterward, they were patched (as shown in the inset) and recorded. (b) Phase-contrast light microscopy image of the primary hippocampal neurons on the photoelectrode. Scale bar is 200 µm. (c) Typical IV-characteristics of the primary hippocampal neurons recorded in the voltage-clamp configuration under dark condition. Inset shows the resting membrane potential distribution for N=10 cells. (d) 3D plots for light-evoked membrane potential modulation in the current-clamp configuration subjected to 5/0.1 ms, 10/0.1 ms and 15/0.1 ms light stimulation (burst waveform), which resulted in action-potential of primary neurons. Increase in duration of ON stimulation also leads to repetitive action potential generation in a continuous burst waveform. For the X axis, each notch in scale represents 100 ms. Each color shows the separate response of distinct neurons. The top panel is the control group that consists of hippocampal cells cultured on a petri dish.

recording was done in current-clamp mode by patching of a single cell in the whole-cell configuration (Fig. 5(a)). The light pulses were illuminated from the top of the surface of the photoelectrode and controlled using an optical set-up as shown in Fig. 5(a). The inset shows the image of a patched primary hippocampal neuron cell during the electrophysiological recording. Figure 5(b) shows phase-contrast light microscopy image of fully grown primary hippocampal cells on the photoelectrode which shows that the neurons are significantly separated, and they have not adequate synaptic connections. Figure 5(c) shows a typical IV characteristic of primary hippocampal cells from the optimized photoelectrode, which was measured in voltage-clamp mode in the dark condition. The cells have quasi-linear response around the resting potential with mean of -68 mV (N=10). Similar to the photocurrent experiments, the electrophysiology is performed in the wireless and free-standing mode, and light pulses at an intensity level of 20 mW.cm^{-2} with a pulse width of 5-ms were used for the photostimulation experiments [1,3]. Before doing the photostimulation experiment with optimized photoelectrode, we used primary hippocampal cells cultured on petri dish as a control experiment. When the light is illuminated on the cells, there was no neural activity as shown in Fig. 5(d). It confirms that the photostimulation of neurons alone do not show any spontaneous activity. However, when the light was illuminated on the photoelectrode with attached neuron cells, the photostimulation is observed which led to the evoking of action potential. The physical mechanism can be explained as the photogenerated electrons travel towards ITO electrode and holes shall be accumulated at the surface close to the attached primary neurons. The hole accumulation leads to a displacement current with a direction from the semiconductor toward the electrolyte. As per our assumption, it leads to hyperpolarization of the attached membrane and depolarization of the free membrane. Since the longer light pulse (5 ms on-time and 5 ms off-time) with square waveform has shown marginal neuromodulation, the action potential was generated when a burst waveform (5 ms on-time and 0.1 ms off-time) was applied (Fig. 5(d)), which has been proposed and demonstrated by Fromherz and co-workers by using electrical stimulation [43]. The burst light pulses can also generate repetitive action potentials at low light intensity levels (Fig. 5(d)). The stimulation is mainly triggered due to the repetitive activation of sodium channels and a summation of small inward currents pulses [43]. Since the photoelectrode has fast switching response (ca. 65 μs light pulses) and the capacitive currents relies on the time-dependent variation of the photovoltage change, it is one of the reasons of photostimulation at low light intensities. Further, the photoelectrode is subjected to 10/0.1 ms and 15/0.1 ms light stimulations (burst waveform) to observe the impact of increased light duration keeping constant off-time. The decrease in number of pulses and repetitive action potential generation are noted with the increase in light exposure time. It is possibly due to the dissipative-interfering currents in the opposite direction while the light exposure time was decreased. Once it reaches threshold voltage, it evokes action potential. The remainder charges available at the photoelectrode surfaces propels for repetitive action potentials in case of higher light on-time. Since some of the visual attributes can only be perceived at threshold for the specific light pulses (in sub-μs region) and train frequency [10,44,45], action potential generation by the weak light intensities could be an interesting finding for the visual prosthesis using photovoltaic photoelectrodes [46].

4. Conclusion

In summary, we demonstrated the optimization of photoelectrodes for efficient transduction of optical signals to currents based on capacitive charge-transfer mechanism. The photoactive layer composed of ternary hybrid of P3HT:PbS QDs:PCBM thin film is optimized in terms of material composition, thin film thickness and morphology in a photocapacitor architecture. The maximum current levels are obtained for the P3HT:PbS QDs:PCBM ratio of 1:0.1:0.5 with thin film thickness of 155 nm and optimized nanomorphology of the thin film surface with a roughness of 1.8 nm. This optimization led to the most efficient photocapacitor with high light sensitivity

that has a photovoltage of 450 mV and a capacitive current of 1.98 mA.cm^{-2} for light intensity level of 20 mW.cm^{-2}. In perspective, controlling the nanomorphology of ternary blends and combination of different hybrid material systems can further facilitate ultra-sensitive capacitive current generation for safe neural prosthesis. Therefore, the results point to an alternative direction in engineering of neural interfaces for effective and safe photostimulation.

Disclosures

"The authors declare no conflicts of interest."

References

1. S. B. Srivastava, R. Melikov, M. M. Aria, U. M. Dikbas, I. H. Kavakli, and S. Nizamoglu, "Band Alignment Engineers Faradaic and Capacitive Photostimulation of Neurons Without Surface Modification," Phys. Rev. Appl. **11**(4), 044012 (2019).
2. D. Rand, M. Jakešová, G. Lubin, I. Vėbraitė, M. David-Pur, V. Đerek, T. Cramer, N. S. Sariciftci, Y. Hanein, and E. D. Głowacki, "Direct Electrical Neurostimulation with Organic Pigment Photocapacitors," Adv. Mater. **30**(25), 1707292 (2018).
3. Y. Jiang, X. Li, B. Liu, J. Yi, Y. Fang, F. Shi, X. Gao, E. Sudzilovsky, R. Parameswaran, K. Koehler, V. Nair, J. Yue, K. Guo, Y. Fang, H.-M. Tsai, G. Freyermuth, R. C. S. Wong, C.-M. Kao, C.-T. Chen, A. W. Nicholls, X. Wu, G. M. G. Shepherd, and B. Tian, "Rational design of silicon structures for optically controlled multiscale biointerfaces," Nat. Biomed. Eng. **2**(7), 508–521 (2018).
4. G. A. Goetz and D. V. Palanker, "Electronic approaches to restoration of sight," Rep. Prog. Phys. **79**(9), 096701 (2016).
5. K. Mathieson, J. Loudin, G. Goetz, P. Huie, L. Wang, T. I. Kamins, L. Galambos, R. Smith, J. S. Harris, A. Sher, and D. Palanker, "Photovoltaic retinal prosthesis with high pixel density," Nat. Photonics **6**(6), 391–397 (2012).
6. M. M. Aria, S. B. Srivastava, E. Sekerdag, U. M. Dikbas, S. Sadeghi, S. R. Pering, P. J. Cameron, Y. Gursoy-Ozdemir, I. H. Kavakli, and S. Nizamoglu, "Perovskite-Based Optoelectronic Biointerfaces for Non-Bias-Assisted Photostimulation of Cells," Adv. Mater. Interfaces **6**(17), 1900758 (2019).
7. H. Bahmani Jalali, O. Karatum, R. Melikov, U. M. Dikbas, S. Sadeghi, E. Yildiz, I. B. Dogru, G. Ozgun Eren, C. Ergun, A. Sahin, I. H. Kavakli, and S. Nizamoglu, "Biocompatible Quantum Funnels for Neural Photostimulation," Nano Lett. **19**(9), 5975–5981 (2019).
8. R. Melikov, S. B. Srivastava, O. Karatum, I. B. Dogru, H. B. Jalali, S. Sadeghi, U. M. Dikbas, B. Ulgut, I. H. Kavakli, and S. Nizamoglu, "Plasmon-Coupled Photocapacitor Neuromodulators," ACS Appl. Mater. Interfaces, 10.1021/acsami.0c09455 (2020).
9. Y. Jiang, R. Parameswaran, X. Li, J. L. Carvalho-de-Souza, X. Gao, L. Meng, F. Bezanilla, G. M. G. Shepherd, and B. Tian, "Nongenetic optical neuromodulation with silicon-based materials," Nat. Protoc. **14**(5), 1339–1376 (2019).

10. S. F. Cogan, "Neural Stimulation and Recording Electrodes," Annu. Rev. Biomed. Eng. **10**(1), 275–309 (2008).
11. B. Tian, S. Xu, J. A. Rogers, S. Cestellos-Blanco, P. Yang, J. L. Carvalho-de-Souza, F. Bezanilla, J. Liu, Z. Bao, M. Hjort, Y. Cao, N. Melosh, G. Lanzani, F. Benfenati, G. Galli, F. Gygi, R. Kautz, A. A. Gorodetsky, S. S. Kim, T. K. Lu, P. Anikeeva, M. Cifra, O. Krivosudský, D. Havelka, and Y. Jiang, "Roadmap on semiconductor–cell biointerfaces," Phys. Biol. **15**(3), 031002 (2018).
12. L. Bareket-Keren and Y. Hanein, "Novel interfaces for light directed neuronal stimulation: advances and challenges," Int. J. Nanomed. **9**(Suppl 1), 65–83 (2014).
13. V. Gaillet, A. Cutrone, F. Artoni, P. Vagni, A. Mega Pratiwi, S. A. Romero, D. Lipucci Di Paola, S. Micera, and D. Ghezzi, "Spatially selective activation of the visual cortex via intraneural stimulation of the optic nerve," Nat. Biomed. Eng. **4**(2), 181–194 (2020).
14. J. F. Maya-Vetencourt, D. Ghezzi, M. R. Antognazza, E. Colombo, M. Mete, P. Feyen, A. Desii, A. Buschiazzo, M. Di Paolo, S. Di Marco, F. Ticconi, L. Emionite, D. Shmal, C. Marini, I. Donelli, G. Freddi, R. Maccarone, S. Bisti, G. Sambuceti, G. Pertile, G. Lanzani, and F. Benfenati, "A fully organic retinal prosthesis restores vision in a rat model of degenerative blindness," Nat. Mater. **16**(6), 681–689 (2017).
15. D. R. Merrill, M. Bikson, and J. G. R. Jefferys, "Electrical stimulation of excitable tissue: design of efficacious and safe protocols," J. Neurosci. Methods **141**(2), 171–198 (2005).
16. I. Schoen and P. Fromherz, "The mechanism of extracellular stimulation of nerve cells on an electrolyte-oxide-semiconductor capacitor," Biophys. J. **92**(3), 1096–1111 (2007).
17. H. Stutzki, F. Helmhold, M. Eickenscheidt, and G. Zeck, "Subretinal electrical stimulation reveals intact network activity in the blind mouse retina," J. Neurophysiol. **116**(4), 1684–1693 (2016).
18. M. Eickenscheidt and G. Zeck, "Action potentials in retinal ganglion cells are initiated at the site of maximal curvature of the extracellular potential," Journal of Neural Engineering **11**(3), 036006 (2014).
19. K. Deisseroth, "Optogenetics: 10 years of microbial opsins in neuroscience," Nat. Neurosci. **18**(9), 1213–1225 (2015).
20. D. Ghezzi, M. R. Antognazza, M. Dal Maschio, E. Lanzarini, F. Benfenati, and G. Lanzani, "A hybrid bioorganic interface for neuronal photoactivation," Nat. Commun. **2**(1), 166 (2011).
21. D. Ghezzi, M. R. Antognazza, R. Maccarone, S. Bellani, E. Lanzarini, N. Martino, M. Mete, G. Pertile, S. Bisti, G. Lanzani, and F. Benfenati, "A polymer optoelectronic interface restores light sensitivity in blind rat retinas," Nat. Photonics **7**(5), 400–406 (2013).
22. G. Simone, D. Di Carlo Rasi, X. de Vries, G. H. L. Heintges, S. C. J. Meskers, R. A. J. Janssen, and G. H. Gelinck, "Near-Infrared Tandem Organic Photodiodes for Future Application in Artificial Retinal Implants," Adv. Mater. **30**(51), 1804678 (2018).
23. V. Gautam, D. Rand, Y. Hanein, and K. S. Narayan, "A Polymer Optoelectronic Interface Provides Visual Cues to a Blind Retina," Adv. Mater. **26**(11), 1751–1756 (2014).
24. V. Gautam, M. Bag, and K. S. Narayan, "Single-Pixel, Single-Layer Polymer Device as a Tricolor Sensor with Signals Mimicking Natural Photoreceptors," J. Am. Chem. Soc. **133**(44), 17942–17949 (2011).
25. M. R. Antognazza, D. Ghezzi, D. Musitelli, M. Garbugli, and G. Lanzani, "A hybrid solid-liquid polymer photodiode for the bioenvironment," Appl. Phys. Lett. **94**(24), 243501 (2009).
26. D. Chen, A. Nakahara, D. Wei, D. Nordlund, and T. P. Russell, "P3HT/PCBM Bulk Heterojunction Organic Photovoltaics: Correlating Efficiency and Morphology," Nano Lett. **11**(2), 561–567 (2011).
27. S. Günes, H. Neugebauer, and N. S. Sariciftci, "Conjugated Polymer-Based Organic Solar Cells," Chem. Rev. **107**(4), 1324–1338 (2007).
28. Q. Li, l. wang, S. Liu, X. Zhan, T. Zhu, Z. Cao, H. Lai, J. Zhao, Y.-P. Cai, W. Xie, and F. Huang, "Impact of Donor–Acceptor Interaction and Solvent Additive on the Vertical Composition Distribution of Bulk-Heterojunction Polymer Solar Cells," ACS Applied Materials & Interfaces (2019).
29. J. Munshi, R. Dulal, T. Chien, W. Chen, and G. Balasubramanian, "Solution Processing Dependent Bulk Heterojunction Nanomorphology of P3HT/PCBM Thin Films," ACS Appl. Mater. Interfaces **11**(18), 17056–17067 (2019).
30. A. G. Pattantyus-Abraham, I. J. Kramer, A. R. Barkhouse, X. Wang, G. Konstantatos, R. Debnath, L. Levina, I. Raabe, M. K. Nazeeruddin, M. Grätzel, and E. H. Sargent, "Depleted-Heterojunction Colloidal Quantum Dot Solar Cells," ACS Nano **4**(6), 3374–3380 (2010).
31. S. A. McDonald, G. Konstantatos, S. Zhang, P. W. Cyr, E. J. D. Klem, L. Levina, and E. H. Sargent, "Solution-processed PbS quantum dot infrared photodetectors and photovoltaics," Nat. Mater. **4**(2), 138–142 (2005).
32. X. Fan, G. Fang, P. Qin, N. Sun, N. Liu, Q. Zheng, F. Cheng, L. Yuan, and X. Zhao, "Deposition temperature effect of RF magnetron sputtered molybdenum oxide films on the power conversion efficiency of bulk-heterojunction solar cells," J. Phys. D: Appl. Phys. **44**(4), 045101 (2011).
33. W. J. D. Beenken, F. Herrmann, M. Presselt, H. Hoppe, S. Shokhovets, G. Gobsch, and E. Runge, "Sub-bandgap absorption in organic solar cells: experiment and theory," Phys. Chem. Chem. Phys. **15**(39), 16494–16502 (2013).
34. V. Sample, S. Ramamurthy, K. Gorshkov, G. V. Ronnett, and J. Zhang, "Polarized activities of AMPK and BRSK in primary hippocampal neurons," Mol. Biol. Cell **26**(10), 1935–1946 (2015).
35. M. L. Seibenhener and M. W. Wooten, "Isolation and culture of hippocampal neurons from prenatal mice," J Vis Exp (2012).
36. A. M. Kleman, J. Y. Yuan, S. Aja, G. V. Ronnett, and L. E. Landree, "Physiological glucose is critical for optimized neuronal viability and AMPK responsiveness in vitro," J. Neurosci. Methods **167**(2), 292–301 (2008).

37. G. Li, V. Shrotriya, Y. Yao, J. Huang, and Y. Yang, "Manipulating regioregular poly(3-hexylthiophene) : [6,6]-phenyl-C61-butyric acid methyl ester blends—route towards high efficiency polymer solar cells," J. Mater. Chem., 17(2007).

38. Z. Jin and J. Wang, "A trilayer architecture for polymer photoconductors," Applied Physics Letters 102(2013).

39. W. Ghann, H. Kang, T. Sheikh, S. Yadav, T. Chavez-Gil, F. Nesbitt, and J. Uddin, "Fabrication, Optimization and Characterization of Natural Dye Sensitized Solar Cell," Sci. Rep. **7**(1), 41470 (2017).

40. L. Ferlauto, M. J. I. Airaghi Leccardi, N. A. L. Chenais, S. C. A. Gilliéron, P. Vagni, M. Bevilacqua, T. J. Wolfensberger, K. Sivula, and D. Ghezzi, "Design and validation of a foldable and photovoltaic wide-field epiretinal prosthesis," Nat. Commun. **9**(1), 992 (2018).

41. N. A. L. Chenais, M. J. I. A. Leccardi, and D. Ghezzi, "Capacitive-like photovoltaic epiretinal stimulation enhances and narrows the network-mediated activity of retinal ganglion cells by recruiting the lateral inhibitory network," J. Neural Eng. **16**(6), 066009 (2019).

42. D. Palanker, A. Vankov, P. Huie, and S. Baccus, "Design of a high-resolution optoelectronic retinal prosthesis," J. Neural Eng. **2**(1), S105–S120 (2005).

43. I. Schoen and P. Fromherz, "Extracellular Stimulation of Mammalian Neurons Through Repetitive Activation of Na+ Channels by Weak Capacitive Currents on a Silicon Chip," J. Neurophysiol. **100**(1), 346–357 (2008).

44. F. T. Hambrecht, "Visual prostheses based on direct interfaces with the visual system," Baillieres Clin Neurol **4**, 147–165 (1995).

45. C. Veraart, C. Raftopoulos, J. T. Mortimer, J. Delbeke, D. Pins, G. Michaux, A. Vanlierde, S. Parrini, and M.-C. Wanet-Defalque, "Visual sensations produced by optic nerve stimulation using an implanted self-sizing spiral cuff electrode," Brain Res. **813**(1), 181–186 (1998).

46. G. Zeck, F. Helmhold, and M. Eickenscheidt, "Receptive field properties in healthy and blind mouse retinas evaluated by stimulation using an implantable subretinal microchip," Invest. Ophthalmol. Visual Sci. **55**, 5966 (2014).